

<https://doi.org/10.1038/s41529-024-00439-9>

Improving HIC resistance of pipe-steel by Ti/Mg treatment with insights into hydrogen migration

Zhixian Peng¹, Jing Liu^{1,2}✉, Rongzhe Hu¹, Shiqi Zhang¹, Feng Huang^{1,3} & Zhengliang Xue¹

The presence of inclusions in steels is responsible for hydrogen-induced cracking (HIC), which necessitates control over their size and distribution. The aims of this study are to investigate the effects of different inclusion-modifying elements on steels, as well as reveal the impact of inclusions on hydrogen migration. Various methods, including HIC evaluation, electrochemical hydrogen permeation, silver microprint, and in-situ hydrogen escape observation, are utilized. The results indicate that steel with a Ti/Mg content ratio of 4:1 exhibits favorable comprehensive resistance against HIC. Moreover, the observation of in-situ hydrogen escape observations reveals that steels with a higher number of hydrogen bubbles and a higher ratio of bubbles related to the inclusions demonstrate better HIC resistance. The refined, dispersed, and multi-compounded inclusions facilitate the formation of more complex trapping sites, ultimately improving the dispersion and pinning of dissociative hydrogen atoms. Consequently, employing a multicomponent inclusion modification strategy holds promise for the development of hydrogen-resistant pipeline steel.

Hydrogen is often regarded as an environmentally superior alternative to conventional fossil fuels in the automotive and power generation sectors^{1,2}. However, atomic hydrogen tends to permeate into materials, leading to hydrogen embrittlement³⁻⁶. The prevailing viewpoint suggests that this embrittlement can be mitigated by incorporating numerous deep hydrogen traps within the materials⁷⁻¹⁰. The underlying principle of this approach aims to immobilize or reversibly bind hydrogen atoms, preventing their capture by relatively weak hydrogen traps such as dislocation strain field, microvoids, and low-angle grain boundaries, which can initiate microcracks¹¹⁻¹⁵. The most employed method for introducing a large number of deep traps in steel materials involves the use of microalloying technology to generate numerous precipitates^{7,9,16,17}. While these dispersed precipitates effectively trap hydrogen, the cost associated with employing microalloy elements must also be considered, particularly in the production of long-term pipeline steel materials.

Modern metallurgical methods have enabled the control of the type, quantity, size, shape, and distribution of inclusions in steel through certain technologies, such as hot metal pretreatment and furnace refining¹⁸⁻²⁰. Shang et al.²¹ studied the inclusions by Ti deoxidation and found that, after Ti treatment of molten steel, the deoxidation products are fine and abundant, potentially becoming the nucleation core of MnS and inhibiting its

aggregation and growth. Nakajima et al.²² concluded that, when Ti-Mg compound deoxidation is adopted, more small-sized composite non-metallic inclusions could be formed in the steel. Furthermore, the inclusions can also promote the formation of acicular ferrite (AF), which is widely considered a HIC resistance promotion factor²³⁻²⁷. Ueshima et al.²⁸ also reported that MnS is prone to nucleate on the surfaces of oxides, and the depletion of Mn content near inclusions can effectively promote the nucleation of acicular ferrite. We previously demonstrated the successful application of Ti-Mg compound deoxidation to create a large number of finely distributed inclusions in steels²⁹⁻³². However, the HIC sensitivities of the steels differ with varying content of Ti-Mg elements addition. Nevertheless, the optimal combination of Ti and Mg elements which can produce superior inclusion morphology with high resistance to HIC still deserves a more comprehensive study. Furthermore, the ideal inclusion design in terms of number, size, and elemental composition remains unclear and warrants further investigation.

This paper seeks to understand the effects of inclusion modification elements on the characterization of inclusions in steel, and the mechanisms by which these inclusions influence the hydrogen migration and segregation, further, the susceptibility of hydrogen-induced cracking (HIC). The nonmetallic inclusions in steel are characterized using field emission

¹The State Key Laboratory of Refractories and Metallurgy, Wuhan University of Science and Technology, 430081 Wuhan, Hubei, China. ²College of Materials Science and Engineering, Shenzhen University, 518000 Shenzhen, China. ³Hubei Engineering Technology Research Centre of Marine Materials and Service Safety, Wuhan University of Science and Technology, 430081 Wuhan, Hubei, China. ✉e-mail: liujing33@szu.edu.cn

scanning electron microscopy (FE-SEM) with energy dispersive spectroscopy (EDS). Dynamic parameters of hydrogen diffusion are measured using electrochemical hydrogen permeation tests. In-situ observation of hydrogen segregation adjacent to inclusions is conducted using the silver microprint technique. Additionally, an in-situ hydrogen escaping device is utilized to investigate hydrogen detraping behavior from the steel. The results of this study can offer researchers a more comprehensive understanding of HIC, and provide steelmakers with a more efficient approach for modifying nonmetallic inclusions. This effort also addresses the need for rapid validation of HIC resistance and incorporation modification efficiency. The goal is to facilitate a swift feedback loop between hydrogen resistance and steelmaking processes, offering a gentle yet effective means of enhancing industry validation practices. Moreover, through a comparative analysis of the efficacy of incorporating deoxidizing elements with regard to HIC resistance and hydrogen permeation properties, we offer insights into recommended strategies for optimizing high-performance anti-HIC pipeline steel.

Results and discussions

Microstructure and inclusions

Figure 1 shows the microstructures of the three test steels observed under an optical microscope (OM). Generally, steels have homogeneous structures without obvious band structure characteristics. As depicted in Fig. 1a–f, the microstructures of the three steels are mainly composed of a large amount of quasi-polygonal ferrite (QF) with a small amount of acicular ferrite (AF) and granular bainite (GB). Comparatively, the average grain sizes of steels 1–3 are ~ 1.2 , ~ 1.3 , and ~ 1.1 μm , respectively.

Figure 2 displays the distributions of inclusions in the three test steels observed under a low magnification of SEM. Overall, the number of inclusions in steel 1 is small, and there is a chain-like distribution of inclusions along the rolling direction. Steel 2 has more inclusions than steel 1, with a certain number of visible irregularly shaped inclusions > 5 μm . Steel 3 exhibits a significant presence of finely dispersed inclusions, characterized by larger inclusions that are smaller than those found in steel 2. These inclusions predominantly assume a spherical shape, contributing to the distinct composition of the steel. Based on the statistical histogram of inclusions depicted in Fig. 3, observed under SEM magnification of $\times 2000$

with over 50 fields, it is evident that steel 1, featuring a Ti/Mg ratio of 0:1, harbors a greater number of Al–Ti–Mg–O–Mn–S complexed inclusions exceeding 3 μm compared to steels 2 and 3. Steel 2 has a certain number of Al–Ti–Mg–O–Mn–S compounded inclusions ranging in size from 1 to 3 μm . Steel 3 has a large number of Si–Al–Ti–Mg–O–Mn–S inclusions within 3 μm with a Ti/Mg addition ratio of 4:1, and the profile of inclusions is spherical as illustrated in Fig. 2, with a relatively uniform distribution and no obvious chain distribution characteristics.

The typical inclusions found in steel 1, as depicted in Fig. 4a, have cores composed of stripes of Ti–Mn–O, which are surrounded by Si–Al–Mg–O–Mn–S compound oxide-sulfides. The sizes of these inclusions range from 1 to 5 μm , and some may even exceed 5 μm . The typical inclusions found in steel 2, as shown in Fig. 4b, contain quasi-spherical inclusions composed of Al–Mg–Ti–O and MnS, with a size range of 1–3 μm . The typical inclusions found in steel 3, with a Ti/Mg addition ratio of 4:1, have many Ti–Si–Mg–O–Mn–S inclusions within 3 μm ; the profile of inclusions is spherical with a relatively uniform distribution and no obvious chain distribution characteristics.

HIC evaluation

The results of the HIC evaluation of the experimental steels are presented in this section. The pH of the solution at the commencement of the immersion test is 2.73, and the pH of the solution at the conclusion is 3.82, which adheres to the requirements of solution pH as stipulated in the standard. According to NACE TM0284-2016, the HIC sensitivity qualification conditions of steel materials are $\text{CLR} \leq 15\%$, $\text{CTR} \leq 3\%$, and $\text{CSR} \leq 1.5\%$ ³³. However, when hydrogen bubbles emerge on the surface of the sample in the HIC sensitivity test, the HIC performance of the sample is deemed unqualified as well³³. Under the magnification of the optical microscope specified in the standard, as listed in Table 1, no internal cracks are observed in the three test steels, indicating that the HIC indexes of the three steels are 0.

Figure 5 shows the macro shoots of three steels after the HIC test. As shown in Fig. 5a, steel 1 exhibits low HIC sensitivity with no internal crack and surface blister. Additionally, steel 1 contains many inclusions, some of which are distributed in long chains. Despite the presence of numerous stripe-shaped inclusions in the steel, there is a considerable amount of

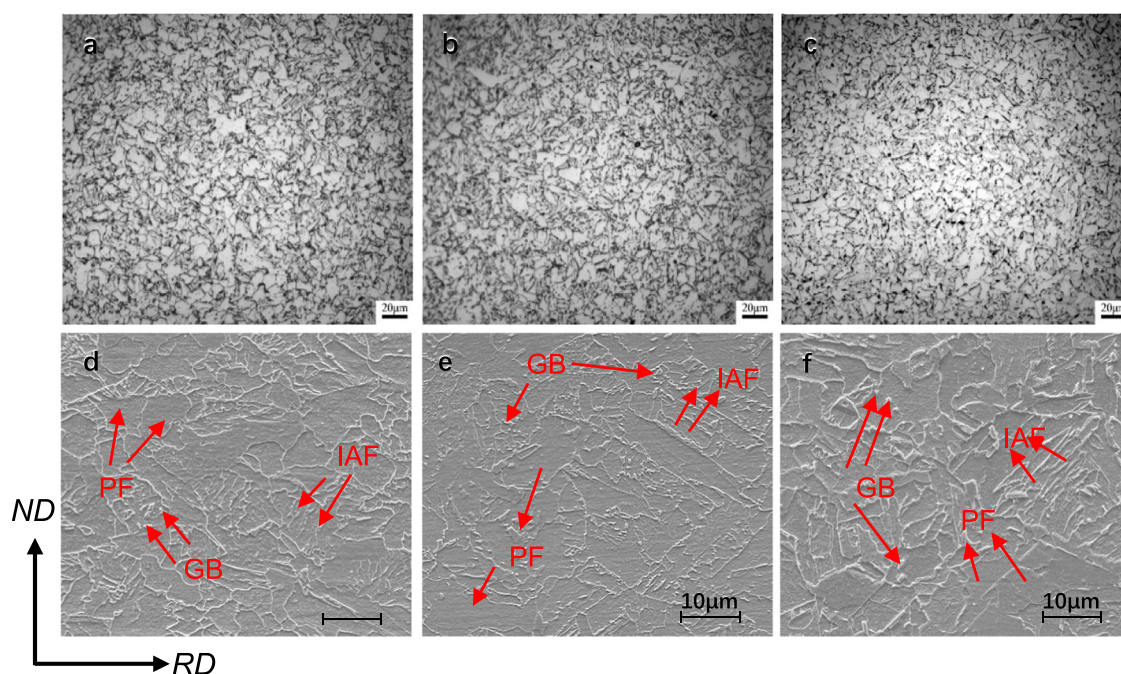


Fig. 1 | Observations on microstructure. Optical microstructure of steels 1 (a), 2 (b), and 3 (c). SEM microstructures of experimental steels 1 (d), 2 (e), and 3 (f). RD means rolling direction, ND means normal direction.

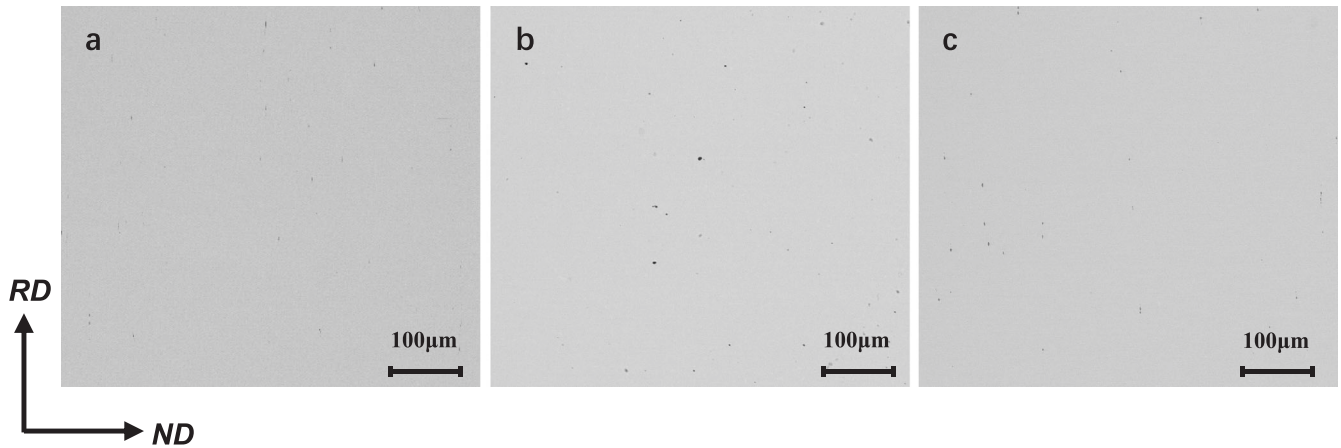


Fig. 2 | Macro distribution of inclusions. SEM morphologies of inclusions at low magnification in steels 1 (a), 2 (b), and 3 (c).

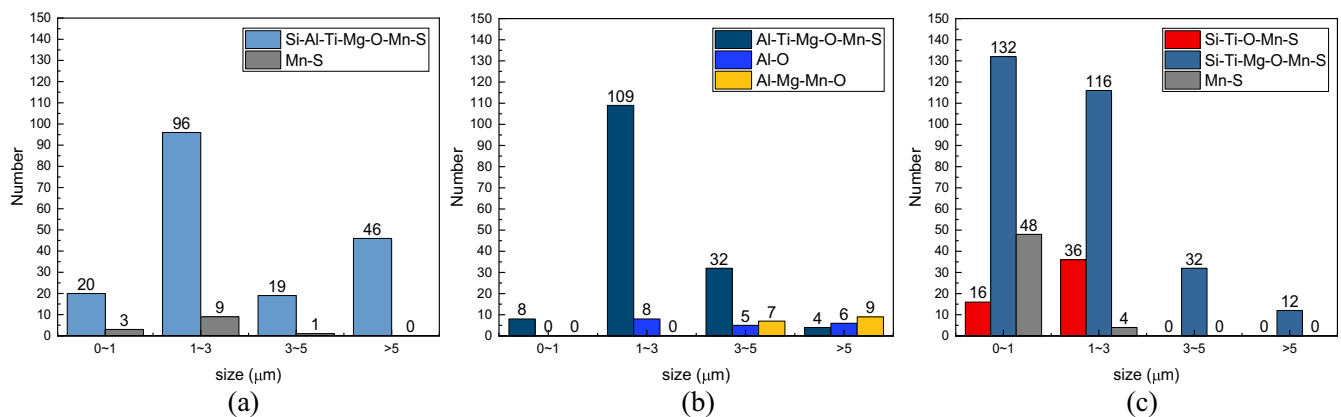


Fig. 3 | Statistic results of inclusions. Distributions of inclusion types, sizes, and quantities in steels 1 (a), 2 (b), and 3 (c).

1–3 μm MnS and oxide-compounded inclusions, which are supposedly capable of dispersing hydrogen atoms and preventing their segregation^{34,35}. For steel 2, when the Ti/Mg addition ratio is 2:1, hydrogen-induced blisters are observed on the material surface after the HIC immersion test, as shown in Figs. 5 and 6, due to the presence of large oxide inclusions. These large oxide inclusions act as hydrogen trappers and provide a place for hydrogen molecule formation. It is evident from Fig. 5b that there are obvious bubbles on the surface of steel 2, which are generally considered hydrogen-induced surface blisters. Additionally, there are a number of microcracks around the main blister crack (marked with red arrows) that are not visible under OM due to its magnification limitation. Figure 6 indicates that a microcrack adjacent to an inclusion is composed of Al–Mg–Mn–O with a size of ~5 μm. The EBSD (electron backscatter diffraction) analysis of local kernel average misorientation (KAM) on the crack field reveals high dislocation densities at the tips of the crack and the boundary of the inclusion^{36,37}.

Hydrogen diffusion and hydrogen trapping

Analysis of Fig. 7 reveals that steel 2 is the first to reach the steady-state platform, followed by steel 1, and steel 3 is the last to reach the steady-state platform. This indicates that the hydrogen atoms in steel 3 need a longer time to reach the saturation state of internal hydrogen traps. The effective hydrogen diffusion coefficient, hydrogen diffusion flux, and cathodic hydrogen concentration were calculated according to the following formulas^{38–40}:

$$D_{\text{eff}} = \frac{L^2}{6t_{0.63}} \quad (1)$$

$$J_{\infty} = \frac{I_{\infty}}{nF} \quad (2)$$

$$C_0 = \frac{J_{\infty}L}{D_{\text{eff}}} \quad (3)$$

where F is Faraday constant, n is charge transfer number, L is sample thickness, I is anode current, I_{∞} is anode saturation current, $t_{0.63}$ is lag time ($I/I_{\infty} = 0.63$), J_{∞} is hydrogen diffusion flux, D_{eff} is effective diffusion coefficient of hydrogen in steel, and C_0 is hydrogen concentration at the cathode side of the sample⁴⁰. The total hydrogen trap density N_T in the sample can be obtained from the following formula⁴¹:

$$N_T = \frac{C_0}{3} \left(\frac{D_L}{D_{\text{eff}}} - 1 \right) \quad (4)$$

where D_L is the diffusion coefficient of hydrogen in lattice sites of iron.

Table 2 further demonstrates that steel 1 has the largest hydrogen diffusion coefficient, while steel 3 with a Ti/Mg ratio of 4:1 has the smallest. Additionally, the hydrogen trap density in steel 3 with a Ti/Mg ratio of 4:1 is the highest, reaching $5.24 \times 10^{19} \text{ m}^{-3}$. This is likely due to the presence of more inclusions in steel 3, which provide more hydrogen traps and impede the diffusion of hydrogen in the steel.

Figure 8 illustrates the macro distribution of the reduced silver particles on the steel surface observed under SEM. As depicted in Fig. 8a and b, a significant number of silver particles are present both in the matrix and adjacent to the inclusions, indicating that the steel matrix and inclusions could act as hydrogen sinks. Conversely, in steel 3, the silver particles are

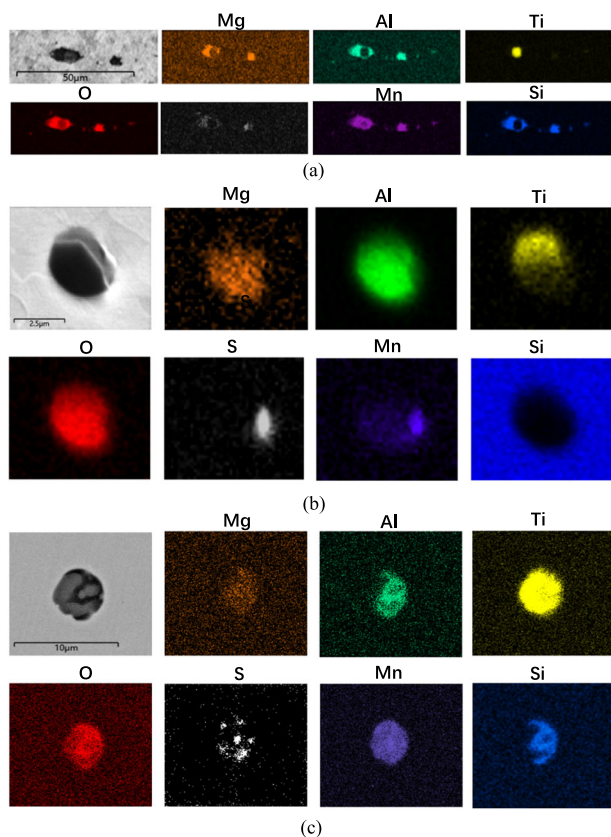


Fig. 4 | SEM and EDS analysis of typical inclusions. Typical inclusion in steels 1 (a), 2 (b), and 3 (c).

Table 1 | Results of HIC tests

	1	2	3
CLR (%)	0	0	0
CTR (%)	0	0	0
CSR (%)	0	0	0
Blisters	\	√	\

more concentrated around the inclusions, and they are scarcely present in the matrix. This trend implies that the hydrogen permeation flux in steel 3 is impeded, leading to the segregation of more hydrogen atoms around the inclusions.

Observations on silver particles around the single inclusions were also conducted under SEM, as depicted in Fig. 9. It shows that a distinct silver particle is adjacent to the Ti–Mg–Al–O–Mn–S, indicating that there were Ag⁺ ions reduced by hydrogen. In the steel matrix next to the inclusion, there are numerous reduced Ag particles. This implies that the hydrogen in the matrix still accounts for a large proportion of the total hydrogen in the steel. In steel 2, a similar phenomenon is observed, with reduced Ag particles present in both the steel and matrix. In contrast, in steel 3, the Ag particles can almost only be seen at the boundary of the inclusions, and no distinct silver particles are observed in the steel matrix. Moreover, silver particles are clearly observed at various locations surrounding the inclusions, suggesting that the inclusions serve as multiple sites for trapping hydrogen.

Figure 10 presents in-situ observations on the diffusion of hydrogen and the formation of hydrogen gas at the surface of steel. The results in Fig. 10b, e and h show that initial hydrogen bubbles were detected around the 11th minute in steel 1, while in steel 2 and 3, the initial hydrogen bubbles were observed at around the 18th and 21st minutes, respectively. This indicates a retardation of hydrogen diffusion flux, which was more

pronounced in steel 3. This finding is consistent with previous electrical permeation test results. As the hydrogen charging process continued, as shown in Fig. 10c, f and i, there was an increase in the number of hydrogen bubbles on the surface of the steels. For instance, at ~15th minutes, there were ~62 hydrogen bubbles in steel 1, while in steel 2 and 3, the time to observe a massive emergence of hydrogen bubbles was ~25th minutes. Moreover, the analysis of the screenshots before and after the bubble formation revealed that in steel 1, the bubbles originated from sites with inclusions (marked with purple arrows), accounting for only 7–9% of the total number of bubbles. Conversely, in steel 2 and 3, the number of hydrogen bubbles was lower, and the bubbles associated with the inclusions (marked with purple arrows) accounted for 28–32% and 62–65% of the total number of bubbles, respectively. It is plausible to speculate that in steel, most of the hydrogen molecules are generated from defects in the steel matrix, such as micro-voids or other types of lower hydrogen bonding defects^{34,42,43}. The inclusions in steel 3 play a significant role in hydrogen distribution and, to some extent, act as hydrogen homogenizers.

Inclusions modification mechanism

Comparing the results of inclusions in steels with different Ti/Mg additions, when the addition of Ti is zero in steel 1, due to the strong deoxidation ability of Mg, it reacts with the original Al₂O₃ and TiO₂ inclusions, and aggregate around the oxides of Ti. The low density of MgO (3.65 g/cm³) and the large contact angle between MgO and molten steel ($\theta = 125^\circ$) make it easy for the original MgO inclusions to form clusters and float in the molten steel, reducing the number of inclusions⁴⁴. Furthermore, the low dissolved oxygen content around the inclusion that arises due to the close-to-equilibrium deoxidation process leads to relatively few secondary deoxidation inclusions formed during cooling and solidification, resulting in reduced inclusion sizes but numbers of nucleation inclusions. As a result, the number of inclusions within the size range of 1–3 µm accounts for a relatively lower proportion, and some of them are distributed in long strip chains, affecting the low-temperature impact toughness of the material; additionally, it is not conducive to the subsequent use of the material.

It is generally accepted that the growth rate of deoxidized inclusions is highly related to the content of dissolved oxygen²³. The relatively high oxygen content in molten steel 2 increases the growth rate of deoxidized inclusions; thus, the sizes of inclusions in steel 2 with a Ti content of 0.0064 wt% are relatively larger than that of steel 3. In steel 3, when Ti/Mg is 4:1, a large number of primary TiO₂ inclusions are generated after increasing the level of Ti deoxidization adding^{45,46}. Due to the low interface energy between Ti deoxidized products and molten iron, this phenomenon increases the homogeneous nucleation rate and number of initial deoxidized inclusions. When the strong deoxidizer Mg is added for further deoxidation, the Mg element will undergo the following three reactions: (1) Mg deoxidizes to form MgO; (2) the reduction of TiO₂ by Mg generates Mg–Ti–O inclusions; and (3) the Mg–Ti–O inclusions precipitate simultaneously, and the inclusions are small and do not easily float in the molten steel⁴⁷. In addition, the addition of more deoxidizing elements in steel 3 leads to the low dissolved oxygen content in molten steel. The initial deoxidized inclusions are restrained from growing up in the Ostwald ripening mode, and the coarsening rate of deoxidized inclusions is delayed⁴⁴. Therefore, the material has the largest number of inclusions, with a large proportion of sizes <1 µm, the inclusion size is small and the distribution is relatively uniform. In terms of controlling sulfides in steel, due to the strong reducibility of Ti and Mg elements at high temperatures, Mn can be replaced by oxides and combined with S atoms in liquid steel. Then, MnS nucleates and adsorbs around oxide inclusions, forming a semi core–shell structure, and inhibiting the aggregation and growth of MnS^{48,49}.

Effects of inclusions on hydrogen redistribution and HIC resistance enhancement

Based on electrochemical tests conducted on steels 1 and 2, it is observed that these steels have a relatively higher diffusion coefficient and lower trap density values than steel 3^{50–52}. This phenomenon can be attributed to the

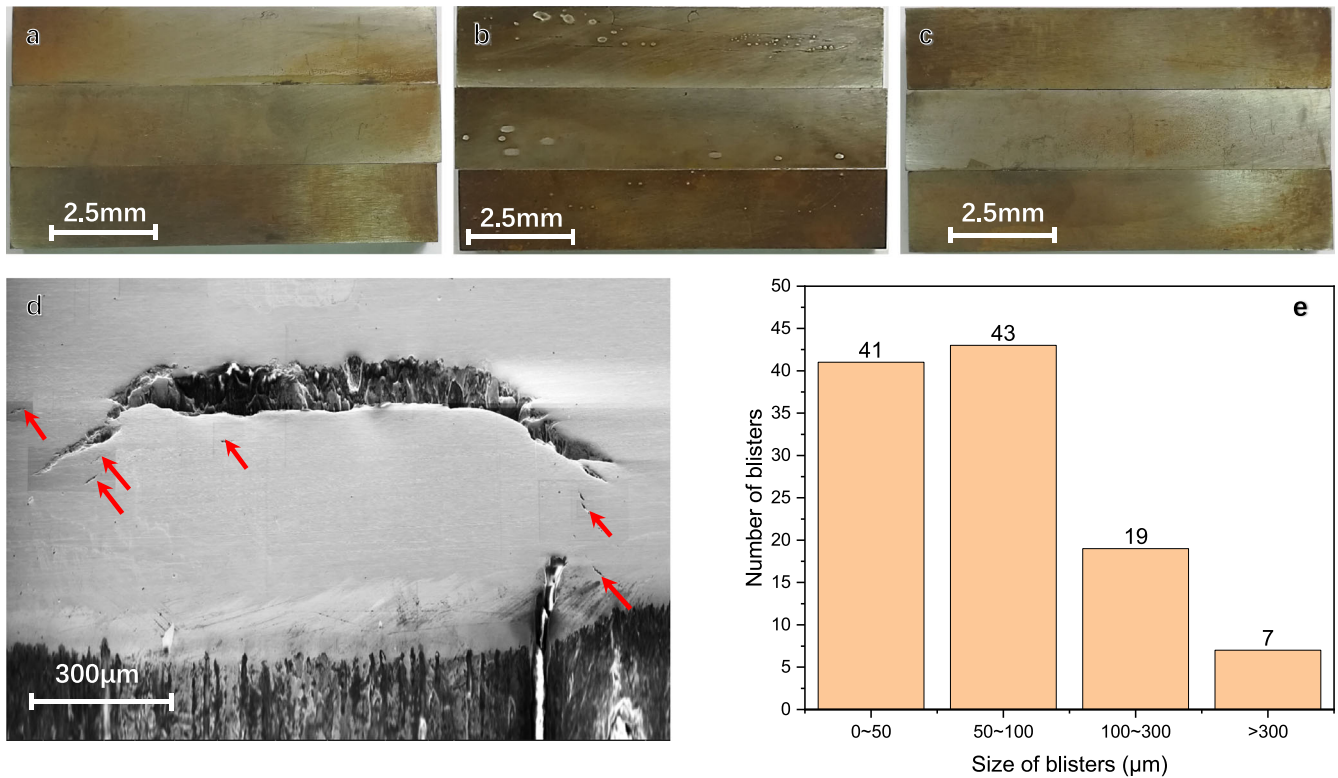


Fig. 5 | Observations on samples after HIC test. Macro shoots of steels 1 (a), 2 (b), and 3 (c) after HIC test; and cross-sectional SEM morphology of the surface blister of steel 2 (d); statistic histogram of average number of blisters with size range in a single specimen of steel 2 (e); arrows in (c) marking the presence of microcracks.

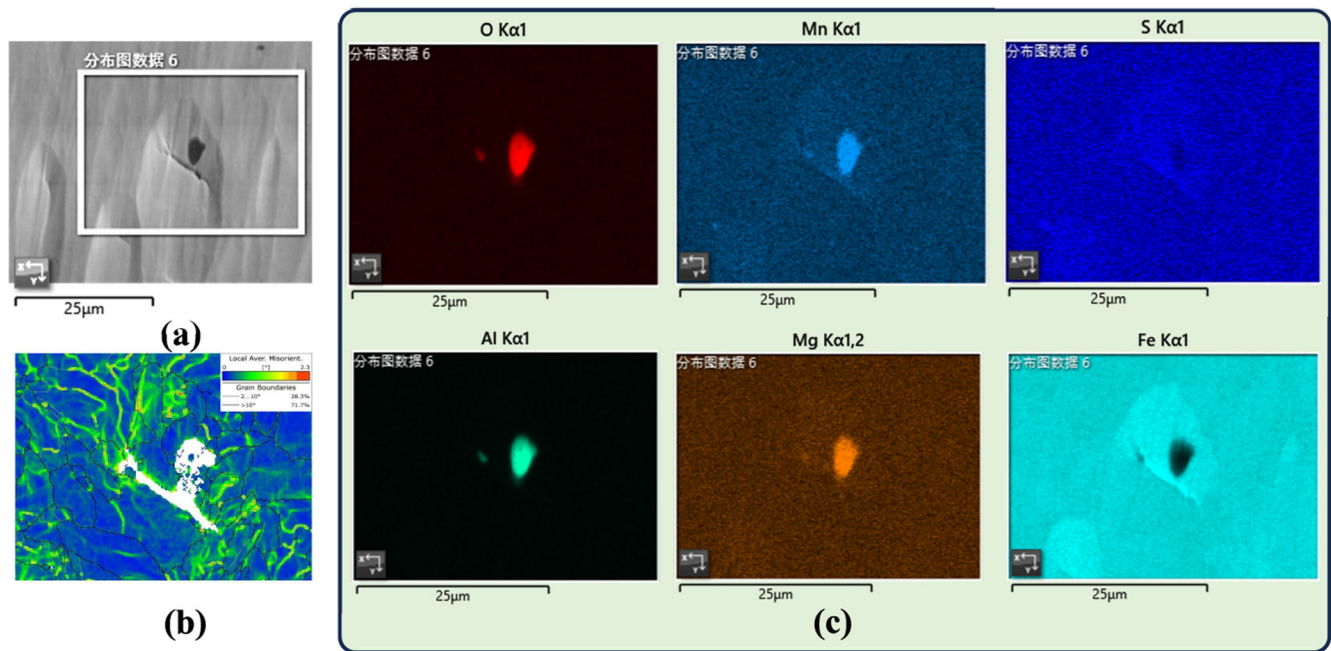
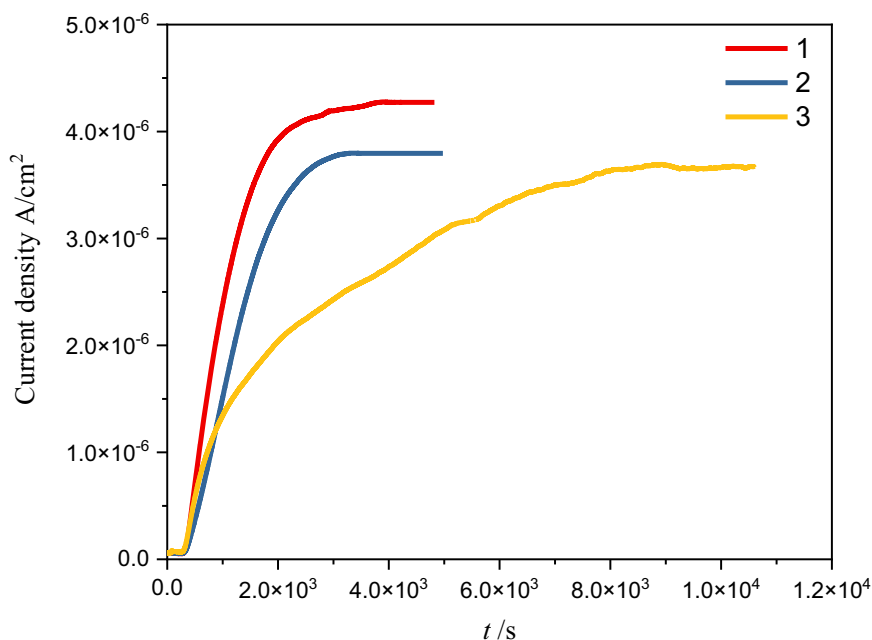


Fig. 6 | Inclusion-induced microcrack in steel 2. SEM photograph (a), KAM map (b), and EDS maps (c).

presence of large inclusions in steel 3. However, it should be noted that coarse inclusions may not possess a good capture effect on hydrogen atoms and may even act as a hydrogen diffusion channel to potential hazard sites³¹. Additionally, the interfaces of most inclusions are either deep hydrogen traps or irreversible hydrogen traps per se^{33,54}. The number of inclusions also reflects the density of hydrogen capturers²⁹⁻³¹. When there are no efficient feasible irreversible hydrogen traps to mediate the

hazard of mobile hydrogen atoms, cracks may occur^{7,16,55}. As a result, significant amounts of hydrogen atoms may still exist in the matrix as reversible hydrogen, as evidenced by the Ag particle reductions shown in Fig. 8 and Fig. 9. The in-situ observations shown in Fig. 10 reveal that for the hydrogen escaping site-related defects in steels 1 and 2, only 7-9% and 28-32% of the total number of bubbles are correlated with the inclusions, respectively. This suggests that the hydrogen atoms in the steel matrix are

Fig. 7 | Hydrogen permeation transient curves of three steels.



not properly guided into the beneficial sites, making steels 1 and 2 increasingly vulnerable to HIC.

However, the situation in steel 3 is unique. The inclusions in steel 3 are finely dispersed, as shown in Fig. 2. The results of hydrogen silver micro-printing, as depicted in Figs. 8 and 9, show that a single inclusion in steel 3 is capable of providing multiple hydrogen traps. The deduced outcomes of N_T , as depicted in Table 2, serve to substantiate the proposed perspective. It is imperative to highlight that the absence of direct evidence for discerning between reversible and irreversible hydrogen entrapment, as observed in thermal desorption spectrometry (TDS) or comparable techniques^{3,29,30,37}, does not undermine the rationality of the drawn conclusion. Consistent with our prior investigations, it is affirmed that dispersed inclusions and their interfacial regions act as proficient irreversible traps, effectively immobilizing mobile hydrogen atoms and thereby mitigating the susceptibility to hydrogen-induced cracking (HIC)³⁹. Additionally, as illustrated in Fig. 10, in-situ hydrogen escape observations reveal that the increased quantity of inclusions not only plays a significant role in hydrogen trapping but also makes a significant difference in hydrogen redistribution to relieve local accumulation in steels, as illustrated in Fig. 11. When hydrogen atoms initially permeate the steel matrix, they tend to diffuse rapidly and gather swiftly around the inclusions, forming a region characterized by a high gradient of hydrogen concentration. This process is sustained with the further motion of hydrogen atoms. After hydrogen diffuses across the material, a channel of hydrogen migration tends to form under the sustained hydrogen charging process, linking the inclusions. On the outer surface of the material, the exposed inclusions (or defects) serve as hydrogen sinks, promoting the recombination of hydrogen atoms into molecules, as illustrated in Fig. 10 and further depicted in Fig. 11d. In the final stage of hydrogen penetration, the inclusions-chaining channel of hydrogen

migration is closely associated with the distribution of inclusions. When inclusions are more dispersed and homogeneous within the matrix, the hydrogen concentration at individual inclusion sites is reduced, lowering the risk of HIC induced by inclusions.

The in-situ observations displayed in Fig. 10 indicate that over 60% of the total number of bubbles related to the hydrogen escaping sites in steel 3 are correlated to the presence of inclusions. These findings strongly support the aspect that finely dispersed inclusions in steel are capable of restoring hydrogen atoms and minimizing the number of reversible hydrogen atoms existing in shallow hydrogen traps, thus reducing the detrimental effects of hydrogen-containing environments on the steel. However, the more comprehensive effect of such modified inclusions should also be addressed. When considering the SEM and EDS maps of the inclusions in Fig. 4, it becomes apparent that inclusions with multipoint heterogeneous sulfide-oxide precipitation can accommodate more hydrogen traps. This finding suggests that a single inclusion has the capacity to trap more hydrogen atoms under multivariate metallurgical construction. Furthermore, the presence of numerous small-sized, multi-composited inclusions in steel 3 plays an important role in capturing and pinning a relatively high number of hydrogen atoms during the hydrogen permeation process, resulting in lower hydrogen diffusion coefficients and higher trap densities. Ultimately, this phenomenon promotes HIC resistance.

Lastly, it is imperative to note that, owing to the inherent limitations of optical microscopy (OM) and scanning electron microscopy (SEM), the in-situ hydrogen escape observation method and the microprint technique are unable to furnish information regarding the trapping effects of nanoscale precipitations, such as carbides or nitrides, on hydrogen atoms. While evidence of their trapping effects has been reported through techniques like atom probe tomography (APT)⁵⁶ and scanning Kelvin probe force microscopy (SKPFM)⁵⁷, the question of whether these precipitations can serve as sites for the accumulation and molecular production of hydrogen atoms remains ripe for further exploration.

In summary, the experimental pipeline steel was produced using the innovative Ti–Mg composite inclusion modification process. The internal inclusions and microstructures of the tested steel, obtained through varying Ti/Mg addition ratios, were meticulously analyzed and discussed. A correlation between the inclusions and hydrogen migration in steels has been discussed. The outcomes of our investigation can be summarized as follows:

Table 2 | Hydrogen diffusion coefficient and hydrogen trap density values of three experimental steels

Steel	1	2	3
D_{eff} ($10^{-6} \text{ cm}^2 \text{ s}^{-1}$)	4.80	3.25	1.77
J_{∞} ($\text{mol cm}^{-1} \text{ S}^{-1}$)	4.42×10^{-11}	3.93×10^{-11}	3.82×10^{-11}
C_0 ($10^{-6} \text{ mol cm}^{-3}$)	1.67	2.15	3.66
N_T (1 m^{-3})	8.55×10^{18}	1.65×10^{19}	5.24×10^{19}

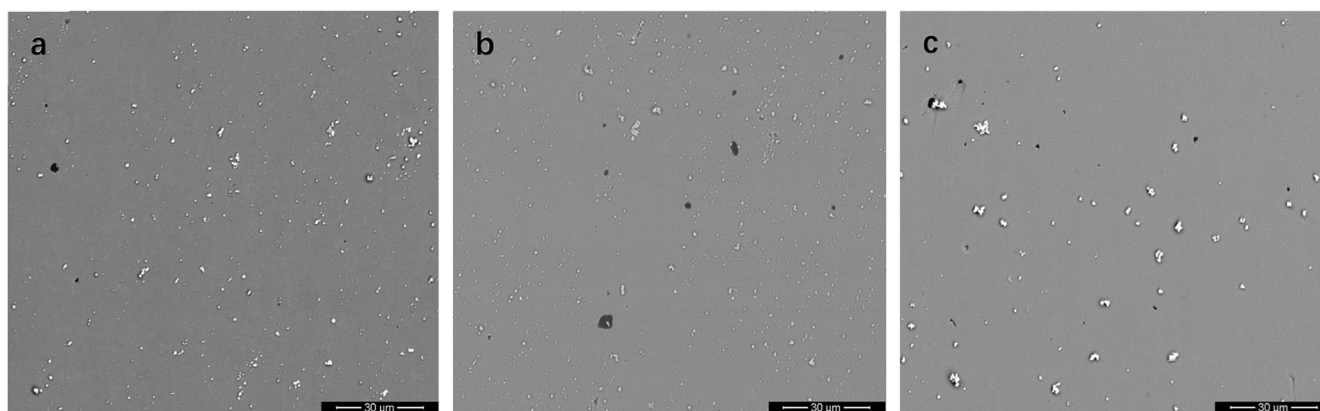


Fig. 8 | SEM observations on samples after hydrogen microprinting treatment. Silver particle distribution of steels 1 (a), 2 (b), and 3 (c).

(1) The steel with a Ti/Mg addition ratio of 4:1 exhibits improved HIC resistance. The higher Ti addition reduces the oxygen concentration in the molten steel, resulting in more finely dispersed particles. Eventually, sulfides nucleate and adsorb around oxides, resulting in the inclusions with a multivariable metallurgical structure.

(2) The presence of multivariate metallurgical construction inclusions allows for the redistribution of hydrogen atoms. These inclusions have the ability to serve as various sites for hydrogen trapping. Additionally, the inclusions can decrease the amount of solution hydrogen in the steel matrix that is available to be trapped by the multicomponent interfaces of the inclusions.

(3) The presence of inclusions in steel has a significant impact on the manner in which hydrogen moves and spreads within the material. The interfaces between inclusions and the steel matrix act as locations where hydrogen atoms get trapped and released. When there are insufficient sites for releasing, the hydrogen atoms accumulate and create localized pressure. This pressure then leads to the formation of tiny voids and eventually cracks. Employing the in-situ observation method for investigation can facilitate the development of a rapid assessment of the HIC sensitivity of steel materials.

Methods

Materials

The designed chemical composition of the experimental steel was based on the framework of X70 pipeline steel, as shown in Table 3. The preparation of the test steel was completed in a pilot plant. The main steps and parameters of the rolling process included heating the steel ingot to 1250 °C and holding it at this temperature for ~2.5 h; the roughing and finishing temperatures were ~1000 °C, the finishing and starting temperatures were ~940 °C and the finishing and finishing temperatures were ~880 °C. After the steel plate was rolled, water was sprayed in the two-phase zone of 700–850 °C for proper and rapid cooling. When the steel plate had cooled to 600 °C, the spraying of water was stopped, and the plate was placed on a stand for air cooling.

Microstructure observations

The observed sample was first wire-cut into dimensions of 20 × 20 × 20 mm, with the observed surface being parallel to the plane of RD⊥ND (RD, rolling direction, ND, normal direction) in the longitudinal section at a distance of 1/4 the width from the rolled plate. The surface of the sample was grounded with abrasive papers and mechanically polished. Subsequently, a metallographic microscope (Zeiss Axioplan 2), scanning electron microscope (FEI Nova Nano 400), and other equipment were used for the observations. For grain size measurement, the standard-based transection method of grain size measurement⁵⁸ was applied. For inclusion statistics, 50 effective fields of view were randomly selected under ×2000 magnification through scanning electron microscopy and energy spectrum analyses. The equivalent radius, number, and composition values of

inclusions were recorded. The sample for the EBSD observation was first mechanically polished, followed by treatment with the Argon ion polishing equipment GATAN PECS II Model 685.

HIC tests

The HIC evaluation tests were conducted according to the NACE TM0284-2016 standard³³. The samples were first cut into the dimensions of 20 × 100 × *T* (thickness of steel sheet) mm, and all the faces of the specimen were then ground with abrasive papers and finished with 320 grids. The NACE A solution with a composition of 5% NaCl + 0.5% CH₃COOH + 94.5% H₂O was applied. Prior to the emersion test, the solution was distilled with high-purity nitrogen for 1 h, followed by induction with high-purity H₂S gas (99.9%). During the induction of H₂S gas, the feed rate was set to 200 mL L⁻¹ min⁻¹ for the first 60 min to ensure a quick saturation of H₂S gas, followed by a feed rate of 100 mL L⁻¹ min⁻¹ to maintain the saturation of H₂S for 95 h. After the HIC test, the samples were taken out and the corrosion products on the surface of the soaked sample were removed, then each tested sample was cut into three parts. The observation surface of the cut sample was ground, polished, observed, and photographed under an optical microscope (magnification of ×100), and the crack length *a* and width *b* were counted. In statistics, cracks with an interval of <0.5 mm were regarded as the same crack, and cracks seen when magnified ×100 under the optical microscope were included. The crack length ratio (CLR), width ratio (CTR), and sensitivity ratio (CSR) were calculated according to formulas (5)–(7). To further observe the change in the internal microstructure of the test steel after the HIC immersion test, the internal cracks of the sample were observed by an optical microscope and scanning electron microscopy.

$$\text{CLR} = \frac{\sum a}{W} \times 100\% \quad (5)$$

$$\text{CTR} = \frac{\sum b}{T} \times 100\% \quad (6)$$

$$\text{CSR} = \frac{\sum (a \times b)}{W \times T} \times 100\% \quad (7)$$

where *a* is the crack length; *b* is the crack thickness; *W* is the section width of the specimen; and *T* is specimen thickness.

Electrochemical hydrogen permeation

The hydrogen permeation experiment was conducted using the modified Devanathan–Stachursky double electrolytic cell, in accordance with the ASTM G148-97 (2018) standard⁵⁹. The specimens were extracted from the rolled sheet along the RD⊥ND plane, measuring 25 × 30 × (1 ± 0.02) mm in dimensions. Subsequently, they underwent double-face polishing and were

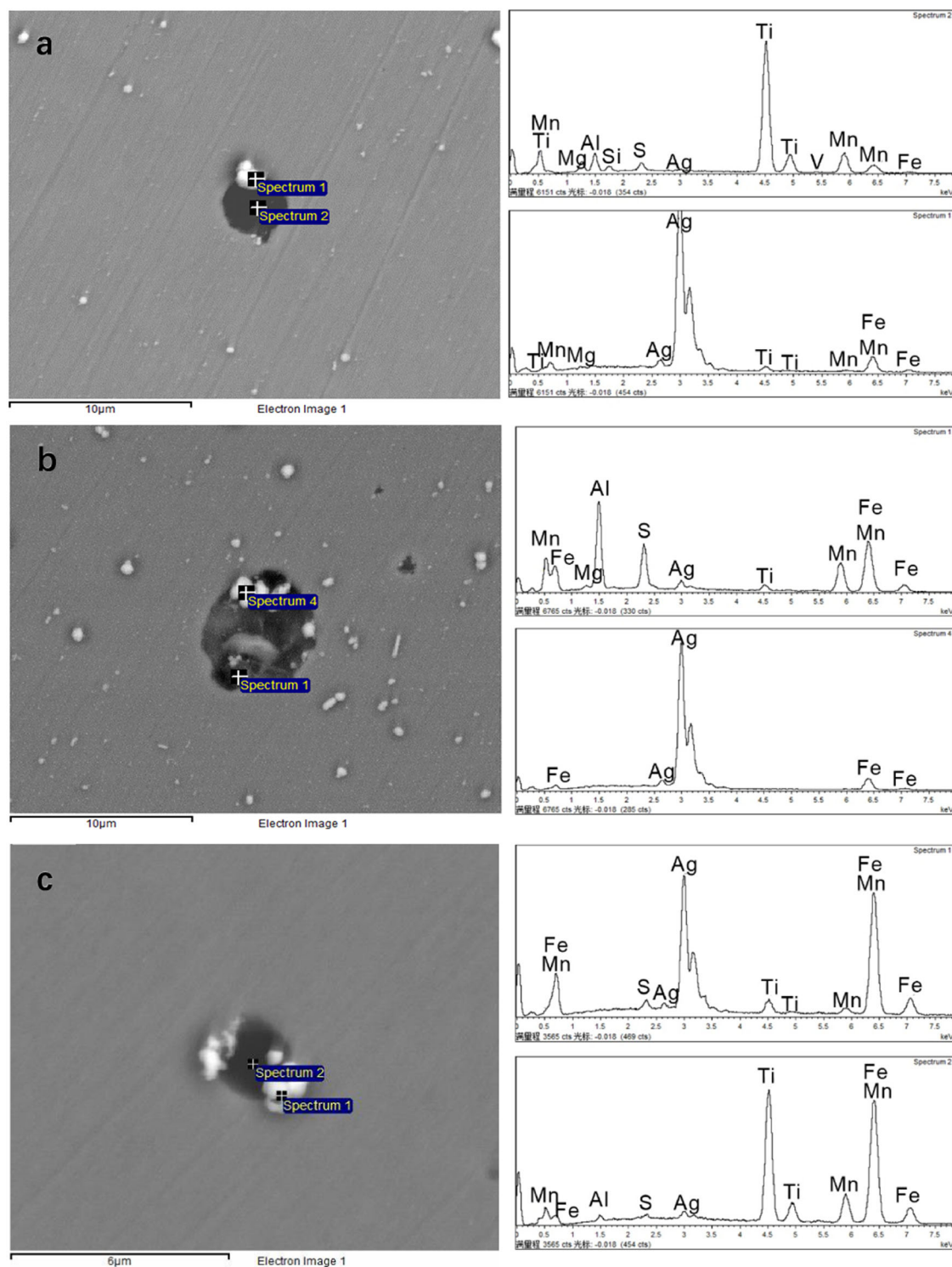


Fig. 9 | Morphology and EDS spectra of single inclusion after hydrogen microprinting treatment. Results of steels 1 (a), 2 (b), and 3 (c).

securely positioned between the cathode and anode chambers, establishing an effective hydrogen charging area of 1 cm^2 . The anode chamber was equipped with a three-electrode system, with a calomel electrode serving as the reference electrode, a platinum electrode serving as the auxiliary electrode, and the sample serving as the working electrode. The three electrodes were connected to the CHI 660A electrochemical workstation via wires. The anode chamber was filled with 0.1 mol/L NaOH solution, and N_2 was continuously introduced for 2 h to remove dissolved oxygen in the solution. Subsequently, the control anode potential was set to $+250\text{ mV}_{\text{SCE}}$, and

when the current density at the back bottom of the anode side decreased to $0.1\ \mu\text{A}/\text{cm}^2$, the cathode side started to apply a hydrogen charging current of $10\text{ mA}/\text{cm}^2$ to the sample in the solution containing $0.5\text{ mol/L H}_2\text{SO}_4$ and 0.2 g/L thiourea . The electrochemical hydrogen permeation curve was obtained by recording the oxidation current at the anode side with the electrochemical workstation. To ensure the reliability of the experimental data, each sample was subjected to at least three hydrogen permeation experiments under the same conditions, and the data curve closest to the average value was selected.

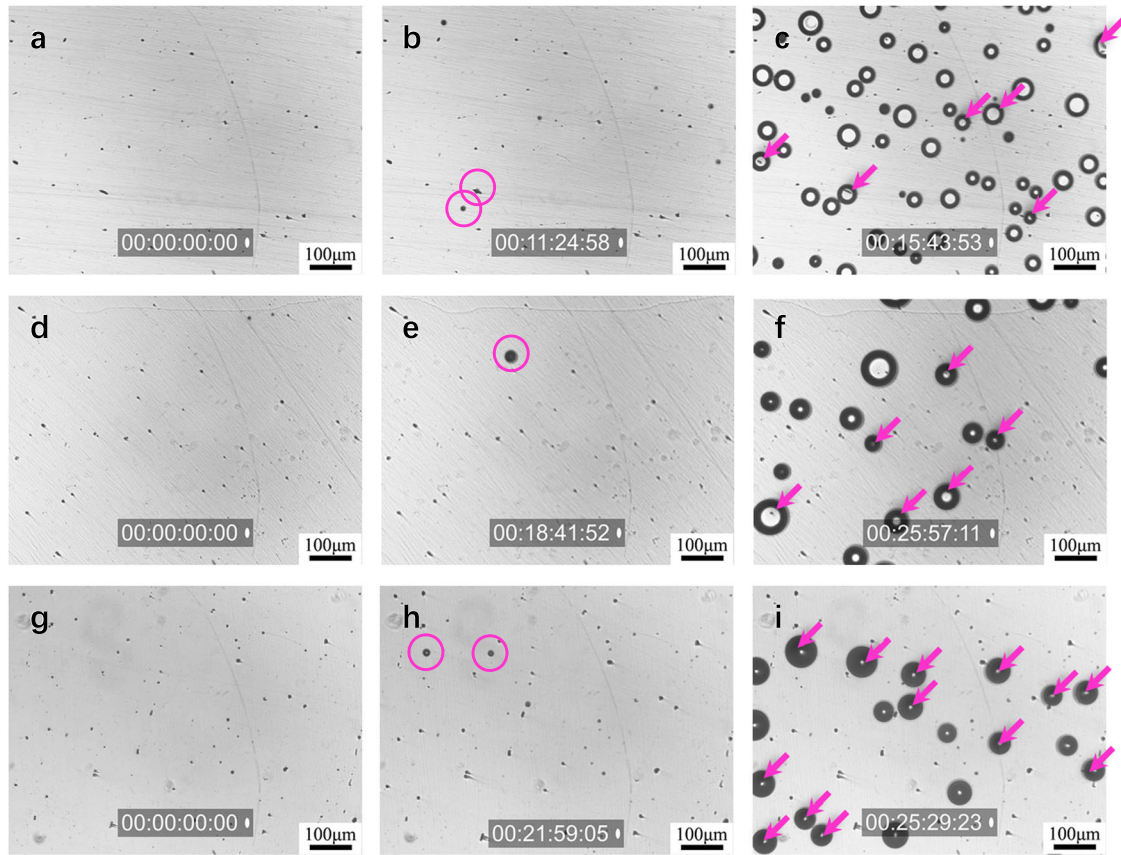


Fig. 10 | In-situ observations on hydrogen bubbling from the surfaces of steels. Microscope screenshots of steels 1 (a–c), 2 (d–f), 3 (g–i); the circular entities depicted in (b), (e), and (h) correspond to the initial bubble formations observed

within three distinct steel specimens; the directional indicators illustrated in (c), (f), and (i) symbolize the emanation of bubbles originating from the inclusion sites within the respective specimens.

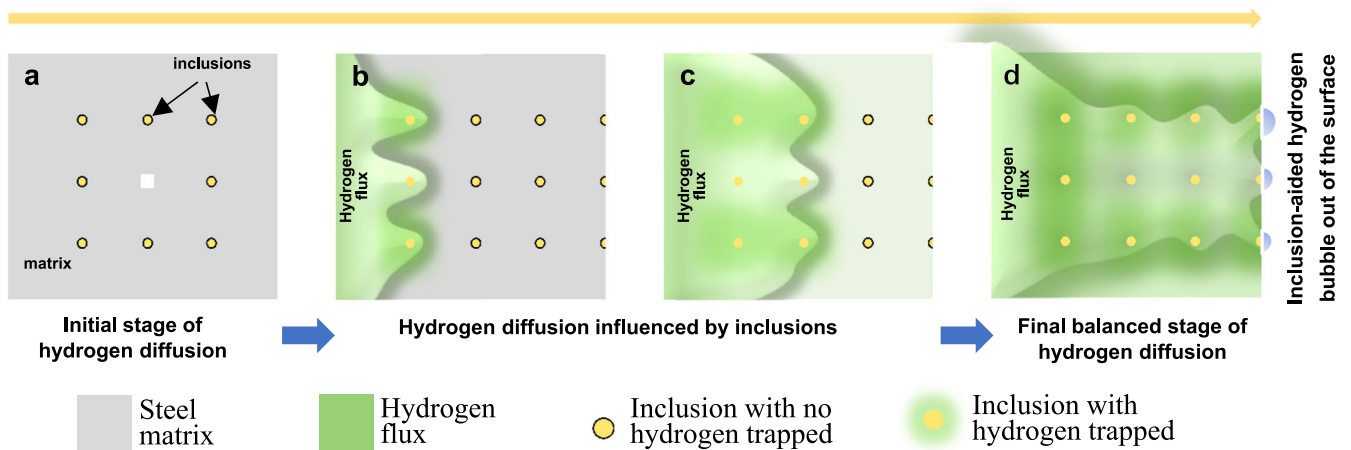


Fig. 11 | Schematic diagram of inclusions affecting hydrogen diffusion and redistribution. Initial stage of hydrogen diffusion (a), hydrogen diffusion influenced by inclusions (b, c), and final balanced stage of hydrogen diffusion (d).

Hydrogen silver microprint technique

The specimen employed in the silver microprint experiment was precisely sectioned to dimensions of 25 × 30 mm parallel to the plane of RD⊥ND, exhibiting a thickness of 1 ± 0.02 mm. The surfaces designated for silver reduction underwent a polishing process to achieve a mirror finish. The silver microprint technique is based on the following redox reaction between absorbed hydrogen atoms and silver ions⁶⁰, $Ag^+ + [H] \rightarrow Ag + H^+$. In this work, a hydrogen microprinting solution and a fixing solution were utilized

Table 3 | Chemical composition of experimental steels (wt%)

Steel	Ti/Mg	C	Si	Mn	P	S	Ti	Mg
1	0:1	0.042	0.25	1.11	0.0045	0.0030	/	0.003
2	2:1	0.044	0.26	1.15	0.0045	0.0030	0.0064	0.003
3	4:1	0.039	0.24	1.10	0.0043	0.0026	0.0120	0.003

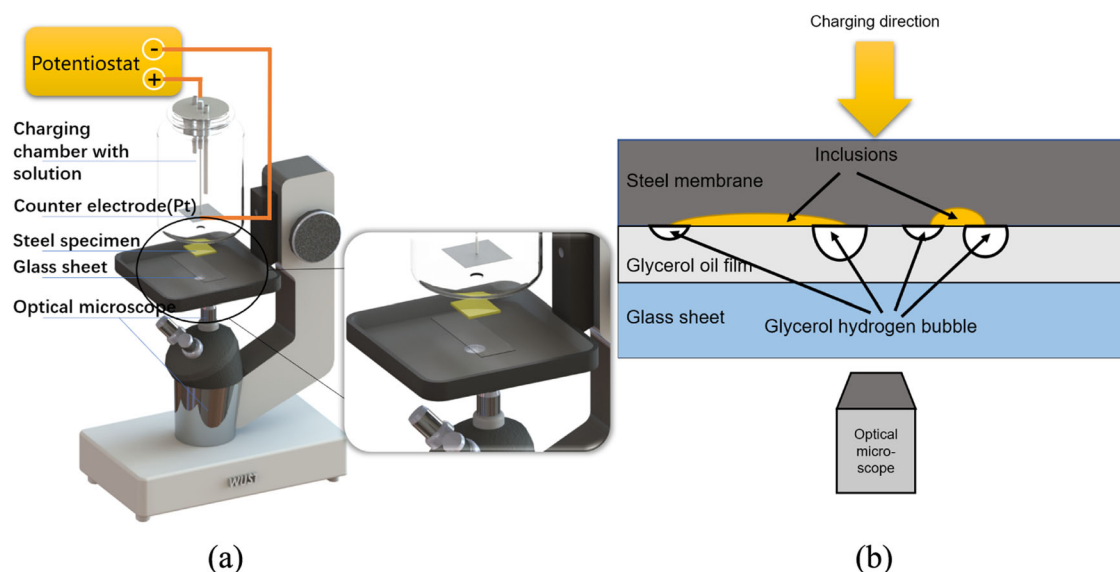


Fig. 12 | Schematic illustration of the device for In-situ hydrogen escape observation. The 3D presentation of the device's assembling (a), illustration of capturing glycerol hydrogen bubbling (b).

in the process of the hydrogen microprinting experiment. The hydrogen microprinting solution was composed of 10 g AgBr nuclear emulsion and 1.4 mol/L sodium nitrite, which was hidden from light during configuration to prevent any adverse effects on the subsequent experiments. The fixing solution is a mixture of 0.6 mol/L sodium thiosulfate and 1.4 mol/L sodium nitrite. After the solutions were prepared, the sample was pre-charged with hydrogen in a water bath pan set at a temperature of 60 °C in the same solution as introduced in the section on electrochemical hydrogen permeation. The hydrogen charging current density was set at 20 mA/cm², and the charging time was limited to 60 min to avoid damaging the sample. Subsequently, the sample was placed in the hydrogen microprint solution for 30 min; then, it underwent 30 min of ultrasonic vibration (UV) in the microprint solution and 20 min of UV in the fixing solution. Finally, the sample was rinsed with alcohol and stored in a drying dish. The samples were repeated at least three times to avoid potential interference from experimental errors, and the results closest to the mean were selected for discussion and analysis.

In-situ hydrogen escape observation

The specimen utilized in the in-situ hydrogen escaping experiment was meticulously sectioned to dimensions measuring 25 × 30 mm parallel to the plane of RD⊥ND, with a thickness of 1 ± 0.02 mm. The in-situ hydrogen escaping from the surface of steel observation was observed using an optical microscope combined with the electrochemical hydrogen charging³⁵. A schematic diagram of the testing device is shown in Fig. 12. During the experiment, the sample was placed between the bottom opening and the glass slide of the hydrogen charging chamber. Glycerol was attached when the glass slide contacted the surface of the sample, and the sample was bonded with the hydrogen charging chamber through silica gel. The magnification used in the observations was ×100. The hydrogen charging solution was a mixture of 0.5 mol/L H₂SO₄ and 0.2 g/L thiourea, and the current density of electrochemical hydrogen charging was 20 mA/cm². The effective hydrogen permeation area was 1 cm². In order to eliminate interference from experimental errors, samples were repeated three times at least and the results closest to the mean were selected for discussion and analysis.

Data availability

All data included in this study are available upon request by contact with the corresponding author.

Received: 28 August 2023; Accepted: 4 February 2024;
Published online: 29 March 2024

References

- Parfomak, P. W. *Pipeline Transportation of Hydrogen: Regulation, Research, and Policy* <https://crsreports.congress.gov/product/pdf/R/R46700> (2021).
- Örnek, C. et al. The causation of hydrogen embrittlement of duplex stainless steel: phase instability of the austenite phase and ductile-to-brittle transition of the ferrite phase—Synergy between experiments and modelling. *Corros. Sci.* **217**, 111140 (2023).
- Meda, U. S., Bhat, N., Pandey, A., Subramanya, K. & Raj, M. L. A. Challenges associated with hydrogen storage systems due to the hydrogen embrittlement of high strength steels. *Int. J. Hydrogen Energy* **48**, 17894–17913 (2023).
- Hoschke, J., Chowdhury, M. F. W., Venezuela, J. & Atrens, A. A review of hydrogen embrittlement in gas transmission pipeline steels. *Corros. Rev.* **41**, 277–317 (2023).
- Sun, H. et al. Optimizing the hydrogen embrittlement resistance by tuning the structures of Cu-rich nanoprecipitates in high strength martensite stainless steels. *Acta Mater.* **246**, 118722 (2023).
- Liu, B. et al. Stress corrosion cracking of X80 steel heat-affected zone in a near-neutral pH solution containing *Bacillus cereus*. *npj Mater. Degrad.* **7**, 27 (2023).
- Kistanov, A. A. et al. Discerning phase-matrices for individual nitride inclusions within ultra-high-strength steel: experiment driven DFT investigation. *Phys. Chem. Chem. Phys.* **24**, 1456–1461 (2022).
- Li, L. F., Song, B., Cheng, J., Yang, Z. & Cai, Z. Effects of vanadium precipitates on hydrogen trapping efficiency and hydrogen induced cracking resistance in X80 pipeline steel. *Int. J. Hydrogen Energy* **43**, 17353–17363 (2018).
- Qiu, X. et al. Investigation of hydrogen diffusion behavior in 12Cr2Mo1R(H) steel by electrochemical tests and first-principles calculation. *Anti-Corros. Methods Mater.* **69**, 17–28 (2021).
- Sznajder, M., Geppert, U. & Dudek, M. R. Hydrogen blistering under extreme radiation conditions. *npj Mater. Degrad.* **2**, 3 (2018).
- Saleh, A. A., Hejazi, D., Gazder, A. A., Dunne, D. P. & Pereloma, E. V. Investigation of the effect of electrolytic hydrogen charging of

- X70 steel: II. Microstructural and crystallographic analyses of the formation of hydrogen induced cracks and blisters. *Int. J. Hydrogen Energy* **41**, 12424–12435 (2016).
12. Turnbull, A. Perspectives on hydrogen uptake, diffusion and trapping. *Int. J. Hydrogen Energy* **40**, 16961–16970 (2015).
13. Xie, D. et al. Hydrogenated vacancies lock dislocations in aluminium. *Nat. Commun.* **7**, 13341 (2016).
14. Qin, W. & Szpunar, J. A. A general model for hydrogen trapping at the inclusion-matrix interface and its relation to crack initiation. *Philos. Mag.* **97**, 3296–3316 (2017).
15. Xu, Y. et al. Study on corrosion, hydrogen permeation, and stress corrosion cracking behaviours of AISI 4135 steel in the tidal zone. *npj Mater. Degrad.* **6**, 96 (2022).
16. Salehin, R., Thompson, G. B. & Weinberger, C. R. Hydrogen trapping and storage in the group IVB–VIB transition metal carbides. *Mater. Design* **214**, <https://doi.org/10.1016/j.matdes.2022.110399> (2022).
17. Chen, W. J., Gao, P. F., Wang, S., Lu, H. Z. & Zhao, Z. Z. Effect of vanadium on hydrogen embrittlement susceptibility of high-strength hot-stamped steel. *J. Iron Steel Res. Int.* **28**, 211–222 (2020).
18. Li, H., Ren, Q. & Zhang, L. Effects of cerium on non-metallic inclusions and rolling contact fatigue life of a high-carbon chromium bearing steel. *Metall. Mater. Trans. A* **54**, 167–178 (2023).
19. Li, H., Ren, Q. & Zhang, L. F. Effect of cerium addition on non-metallic inclusions in a high-carbon chromium bearing steel. *J. Iron Steel Res. Int.* **30**, 2254–2266 (2023).
20. Cheng, W., Song, B. & Mao, J. Effect of Ce content on the hydrogen induced cracking of X80 pipeline steel. *Int. J. Hydrogen Energy* **48**, 15303–15316 (2023).
21. Shang, D., Lv, C. & Yu, G. Precipitation and growth of oxides during solidification of titanium deoxidized low carbon steel. *Casting* **57**, 553–556 (2008).
22. Nakajima, K., Ohta, H., Suito, H. & Jönsson, P. Effect of oxide catalyst on heterogeneous nucleation in Fe–10mass% Ni alloys. *ISIJ Int.* **46**, 807–813 (2006).
23. Li, X. B., Zhang, T. S., Min, Y., Liu, C. G. & Jiang, M. F. Effect of magnesium addition in low carbon steel part 2: toughness and microstructure of the simulated coarse-grained heat-affected zone. *Ironmak. Steelmak.* **46**, 301–311 (2019).
24. Yang, S. F., Li, J. S., Wang, Z. F., Li, J. & Lin, L. Modification of MgO–Al₂O₃ spinel inclusions in Al-killed steel by Ca-treatment. *Int. J. Miner. Metall. Mater.* **18**, 18–23 (2011).
25. Zhang, C. J., Gao, L. N. & Zhu, L. G. Effect of inclusion size and type on the nucleation of acicular ferrite in high strength ship plate steel. *ISIJ Int.* **58**, 965–969 (2018).
26. Lin, G. H. *Pipeline Steel and Pipeline Steel Pipe* (China Petrochemical Press, 2012).
27. Ge, Q. R., Chen, J., Wang, B., Liu, Q. Y. & Gan, G. Y. Effect of microstructure on hydrogen-induced cracking behavior of ultra-low carbon X80 pipeline steel. *Mech. Eng. Mater* **41**, 20–24 (2017).
28. Ueshima, Y., Yuyama, H., Mizoguchi, S. & Kajioaka, H. Effect of oxide inclusions on MnS precipitation in low carbon steel. *Tetsu-to-Hagané* **75**, 501–508 (1989).
29. Peng, Z. X. et al. Comparative study of non-metallic inclusions on the critical size for HIC initiation and its influence on hydrogen trapping. *Int. J. Hydrogen Energy* **45**, 12616–12628 (2020).
30. Peng, Z. X. et al. Effect of submicron-scale MnS inclusions on hydrogen trapping and HIC susceptibility of X70 pipeline steels. *Steel Res. Int.* **89**, 1700566 (2018).
31. Peng, Z. X. et al. The significance of inclusion morphology and composition in governing hydrogen transportation and trapping in steels. *Int. J. Hydrogen Energy* **46**, 28811–28822 (2021).
32. Xiao, H., Huang, F., Peng, Z. X., Fan, L. X. & Liu, J. Sequential kinetic analysis of the influences of non-metallic inclusions on hydrogen diffusion and trapping in high-strength pipeline steel with Al–Ti deoxidisation and Mg treatment. *Corros. Sci.* **195**, 110006 (2022).
33. NACE Standard TM 0284–2016. *Standard Test Method Evaluation of Pipeline and Pressure Vessel Steels for Resistance to Hydrogen-Induced Cracking* (NACE International, Houston, TX, 2016).
34. Huang, F. et al. Effect of microstructure and inclusions on hydrogen induced cracking susceptibility and hydrogen trapping efficiency of X120 pipeline steel. *Mater. Sci. Eng.: A* **527**, 6997–7001 (2010).
35. Peng, Z. et al. The significance of inclusion morphology and composition in governing hydrogen transportation and trapping in steels. *Int. J. Hydrogen Energy* **46**, 28811–28822 (2021).
36. Fu, Y. et al. Hydrogen induced microstructure, mechanical properties and cracking evolution in a novel CoCrNiMo medium-entropy alloy. *J. Alloy. Compd.* **939**, 168790 (2023).
37. Zhang, S. et al. The significant effect of tantalum on the hydrogen-induced cracking of pipeline steel: Morphology, hydrogen permeation, and theoretical studies. *Corros. Sci.* **200**, 110213 (2022).
38. Huang, F. et al. Hydrogen-induced cracking susceptibility and hydrogen trapping efficiency of different microstructure X80 pipeline steel. *J. Mater. Sci.* **46**, 715–722 (2011).
39. Luu, W. C. & Wu, J. K. Effects of sulfide inclusion on hydrogen transport in steels. *Mater. Lett.* **24**, 175–179 (1995).
40. Gesnoui, C. et al. Effect of post-weld heat treatment on the microstructure and hydrogen permeation of 13CrNiMo steels. *Corros. Sci.* **46**, 1633–1647 (2004).
41. Li, Y. F., Cai, L., Kan, W. B. & Akiyama, E. Permeation and diffusion characteristics of hydrogen in low carbon steel. *J. East China Univ. Sci. Technol.* **39**, 222–227 (2013).
42. Dong, C. F., Li, X. G., Liu, Z. Y. & Zhang, Y. R. Hydrogen-induced cracking and healing behaviour of X70 steel. *J. Alloy. Compd.* **484**, 966–972 (2009).
43. Gu, C., Lian, J., Bao, Y., Xiao, W. & Münstermann, S. Numerical study of the effect of inclusions on the residual stress distribution in high-strength martensitic steels during cooling. *Appl. Sci.* **9**, <https://doi.org/10.3390/app9030455> (2019).
44. Karasev, A. V. & Suito, H. Characteristics of fine oxide particles produced by Ti/M (M = Mg and Zr) complex deoxidation in Fe–10mass% Ni alloy. *ISIJ Int.* **48**, 1507–1516 (2008).
45. Zhang, T., Liu, C. & Jiang, M. Effect of Mg on behavior and particle size of inclusions in Al–Ti deoxidized molten steels. *Metall. Mater. Trans. B* **47**, 2253–2262 (2016).
46. Zhong, H. et al. Formation and evolution of non-metallic inclusions in X70MS pipeline steel during LF–RH–CC process. *Metall. Res. Technol.* **119**, 522 (2022).
47. Ming, L. X., Shaobo, Z. & Qing, Z. Oxide metallurgy technology of steel. *Shanghai Met.* **27**, 55–60 (2005).
48. Kim, H. S., Lee, H. G. & Kyung Shik, O. Precipitation behavior of MnS on oxide inclusions in Si/Mn deoxidized steel. *Met. Mater.* **6**, 305–310 (2000).
49. Kim, H. S., Lee, H. G. & Oh, K. S. MnS precipitation in association with manganese silicate inclusions in Si/Mn deoxidized steel. *Metall. Mater. Trans. A* **32**, 1519 (2001).
50. Lin, J., Liu, Y. & Dean, T. A. Investigation of Damage Features In Hot Metal Forming. *AIP Conf. Proc. (Bridget D’Amelio)* **712**, 1851–1856 (2004).
51. Varanasi, R. S., Koyama, M., Shibayama, Y. & Akiyama, E. Mixed type brittle fracture in 1.5 GPa dual-phase steel via {100} ferrite cleavage cracking. *Mater. Sci. Eng.: A* **857**, 144021 (2022).
52. Ma, M. T. et al. Hydrogen embrittlement of advanced high-strength steel for automobile application: a review. *Acta Metall. Sin. (English Lett.)* **36**, 1144–1158 (2023).

53. Ohaeri, E. G., Qin, W. & Szpunar, J. A critical perspective on pipeline processing and failure risks in hydrogen service conditions. *J. Alloy. Compd.* **857**, 158240 (2021).
54. Guedes, D. et al. The role of plasticity and hydrogen flux in the fracture of a tempered martensitic steel: a new design of mechanical test until fracture to separate the influence of mobile from deeply trapped hydrogen. *Acta Mater.* **186**, 133–148 (2020).
55. Li, L., Song, B., Cheng, J., Yang, Z. & Cai, Z. Effects of vanadium precipitates on hydrogen trapping efficiency and hydrogen induced cracking resistance in X80 pipeline steel. *Int. J. Hydrogen Energy* **43**, 17353–17363 (2018).
56. Chen, Y.-S. et al. Direct observation of individual hydrogen atoms at trapping sites in a ferritic steel. *Science* **355**, 1196–1199 (2017).
57. Zhang, B. et al. Atomic-scale insights on hydrogen trapping and exclusion at incoherent interfaces of nanoprecipitates in martensitic steels. *Nat. Commun.* **13**, 3858 (2022).
58. Committee, N. S. M. *Determination of Estimating the Average Grain Size of Metal* GB/T 6394–2017 (China Standard Press, Beijing, 2017).
59. Standard, A. S. T. M. *Standard Practice for Evaluation of Hydrogen Uptake, Permeation, and Transport in Metals by an Electrochemical Technique* ASTM G148–97 (ASTM International, West Conshohocken, 2018).
60. Ovejero-García, J. Hydrogen microprint technique in the study of hydrogen in steels. *J. Mater. Sci.* **20**, 2623–2629 (1985).

Acknowledgements

This work is funded by National Natural Science Foundations of China (52231003, 52201084), Major Program (JD) of Hubei Province (2023BAA019), Petro China Innovation Foundation (No. 2020D-5007-0311), Natural Science Foundation of Hubei Province of China (2022CFC007), Postdoctoral Station of Metallurgical Engineering of Wuhan University of Science and Technology, Postdoctoral Workstation of Zhejiang Jincheng New Material Co., Ltd. This work also thanks to the Analysis and Testing Centre of Wuhan University of Science and Technology.

Author contributions

Z.X. Peng: conceptualization and methodology, original manuscript writing, experimental work, data interpretation. R.Z. Hu: experimental work, data interpretation. S.Q. Zhang, F. Huang, and Z.L. Xue: manuscript review and editing. J. Liu: program management, manuscript review, and editing.

Competing interests

The authors declare no competing interests.

Additional information

Correspondence and requests for materials should be addressed to Jing Liu.

Reprints and permissions information is available at <http://www.nature.com/reprints>

Publisher's note Springer Nature remains neutral with regard to jurisdictional claims in published maps and institutional affiliations.

Open Access This article is licensed under a Creative Commons Attribution 4.0 International License, which permits use, sharing, adaptation, distribution and reproduction in any medium or format, as long as you give appropriate credit to the original author(s) and the source, provide a link to the Creative Commons licence, and indicate if changes were made. The images or other third party material in this article are included in the article's Creative Commons licence, unless indicated otherwise in a credit line to the material. If material is not included in the article's Creative Commons licence and your intended use is not permitted by statutory regulation or exceeds the permitted use, you will need to obtain permission directly from the copyright holder. To view a copy of this licence, visit <http://creativecommons.org/licenses/by/4.0/>.

© The Author(s) 2024